

Irreversibility in Bacterial Turbulence: Insights from the Mean-Bacterial-Velocity Model

Kolluru Venkata Kiran,^{1,*} Anupam Gupta,^{2,†} Akhilesh Kumar Verma,^{3,‡} and Rahul Pandit^{4,§}

¹*Centre for Condensed Matter Theory, Department of Physics,
Indian Institute of Science, Bangalore, 560012, India.*

²*Department of Physics, Indian Institute of Technology (IIT),
Hyderabad, Kandi Sangareddy Telangana, 502285, India*

³*Mathematics Institute, Zeeman Building, University of Warwick, Coventry CV4 7AL, UK*

⁴*Centre for Condensed Matter Theory, Department of Physics,
Indian Institute of Science, Bangalore, 560012, India.*

We use the mean-bacterial-velocity model to investigate the *irreversibility* of two-dimensional (2D) *bacterial turbulence* and to compare it with its 2D fluid-turbulence counterpart. We carry out extensive direct numerical simulations of Lagrangian tracer particles that are advected by the velocity field in this model. Our work uncovers an important, qualitative way in which irreversibility in bacterial turbulence is different from its fluid-turbulence counterpart: For large positive (or large but negative) values of the *friction* (or *activity*) parameter, the probability distribution functions of energy increments, along tracer trajectories, or the power are *positively* skewed; so irreversibility in bacterial turbulence can lead, on average, to *particles gaining energy faster than they lose it*, which is the exact opposite of what is observed for tracers in 2D fluid turbulence.

Most fluid flows are turbulent; and they can attain a nonequilibrium, but statistically steady, state (NESS), if the energy injection into the fluid, say by an external force, is balanced by viscous dissipation. Far away from boundaries, this NESS is statistically homogeneous and isotropic if we consider length scales that are much smaller than the energy-injection scale l_f [1, 2]. Two important characteristics of this NESS are (a) the distribution of energy over a large range of length scales and (b) the temporal irreversibility of turbulent flows. This irreversibility is not easily apparent if we look at movies, played forward or backward in time, of Lagrangian particles, or *tracers*, that are advected by turbulent flows; however, the statistics of such tracers or inertial particles in turbulent flows yields signatures of this irreversibility [3–10]: if we analyse (a) the increments

$$W(t, \tau) \equiv E(t + \tau) - E(t) \quad (1)$$

of the particle energy E at time t or (b) the power

$$p_L(t) \equiv \frac{dE}{dt} = a_L v_L, \quad (2)$$

with v_L the magnitude of the tracer velocity and a_L the component of its acceleration along its trajectory. It has been found that probability distribution functions (PDFs) of W and p_L , obtained

by averaging over t and the trajectories of all tracers, are negatively skewed [3, 7, 9, 11–14]; i.e., on average, such tracers lose energy faster than they gain it. Is it possible to use these PDFs to characterise irreversibility in *bacterial turbulence* [15–22]? We show that this can, indeed, be done. We illustrate this by carrying out an extensive study of the irreversibility of bacterial turbulence in the mean-bacterial-velocity model [15]. Our work uncovers an important, qualitative way in which irreversibility in bacterial turbulence is different from its fluid-turbulence counterpart: For large positive (or large but negative) values of the *friction* (or *activity*) parameter α (see below), the PDFs of $W(\tau)$ or p_L are *positively* skewed; this implies that irreversibility in bacterial turbulence can lead, on average, to *particles gaining energy faster than they lose it*, for certain ranges of values of α .

Dense bacterial suspensions, which are examples of active systems [15, 16, 20, 23–25], show spatiotemporal evolution that is reminiscent of flows in turbulent fluids. Hydrodynamical models have been developed to describe turbulence in dense, quasi-two-dimensional (2D) bacterial suspensions [17–21, 24, 26, 27]. We use the mean-bacterial-velocity model [15] or the Toner-Tu-Swift-Hohenberg (TTSH) model [25, 28], for the incompressible velocity field $\mathbf{u}(\mathbf{x}, t)$; this model has been employed to study turbulence in dense sus-

pensions of *B. subtilis*:

$$\begin{aligned} \frac{\partial \mathbf{u}}{\partial t} + \lambda_0 \mathbf{u} \cdot \nabla \mathbf{u} &= -\nabla P - (\alpha + \beta |u|^2) \mathbf{u} \\ &+ \Gamma_0 \nabla^2 \mathbf{u} - \Gamma_2 \nabla^4 \mathbf{u}; \\ \nabla \cdot \mathbf{u} &= 0. \end{aligned} \quad (3)$$

Here, $P(\mathbf{x}, t)$ is the pressure at point \mathbf{x} and time t ; the constant density ρ is set to unity [29]. We use periodic boundary conditions in all directions because we concentrate on statistically homogeneous and isotropic bacterial turbulence. We restrict ourselves to two dimensions (2D) as most experiments in this field have been conducted in quasi-2D systems.

The parameters $\Gamma_0 < 0$ and $\Gamma_2 < 0$; a spatial Fourier transform of Eq. (3), followed by a linear-stability analysis about the spatially uniform state, yields the wave vectors \mathbf{k} , with magnitude k , for which there are linearly unstable modes. We define the following characteristic length, velocity, and time scales, respectively:

$$\Lambda = 2\pi \sqrt{\frac{2\Gamma_2}{\Gamma_0}}; v_0 = \sqrt{\frac{|\Gamma_0|^3}{\Gamma_2}}; \theta = \frac{\Lambda}{v_0}. \quad (4)$$

These unstable modes provide a source of energy injection into the system [30]; this energy is dissipated by (a) the linearly stable modes, (b) the cubic term with the coefficient $\beta > 0$, and (c) the linear term with the coefficient α , if $\alpha > 0$. Moreover, there is energy injection, or *activity*, if $\alpha < 0$; and $\Gamma_0 < 0$ and $\lambda_0 \neq 1$ also induce activity [28] [$\lambda_0 > 1$ for *pusher swimmers* like *B. subtilis* (see, e.g., Refs. [15, 16, 31])]. The interplay between these energy-injection and dissipation terms leads to a NESS with self-sustained, turbulence-type patterns [22]. The effective viscosity

$$k^2 \nu_{eff}(k) = (\alpha + 2\beta u_{rms}^2 + \Gamma_0 k^2 + \Gamma_2 k^4) \quad (5)$$

can be used to rewrite Eq. (3) in a Navier-Stokes form (see the Supplemental Material and Ref. [22]). Clearly, the wave numbers k at which energy is injected (dissipated) are those with $\nu_{eff}(k) < 0$ (> 0); the root-mean-square velocity u_{rms} must be obtained from a calculation (see below).

We solve Eq. (3) by a pseudospectral direct numerical simulation (DNS) [see, e.g., Ref. [32]] with $N^2 = 1024^2$ collocation points and the parameters in Table I; we have checked in representative cases that our results are unchanged if we use

Run	Γ_2	α	δt	Λ	θ	v_0
A1-A12	9e-5	*	2e-4	0.40	0.40	1.0
B	9e-5	-4	1e-5	0.40	0.40	1.0
C	9e-5	1	5e-5	0.40	0.40	1.0
D	3.6e-5	14	1e-4	0.25	0.16	1.60

TABLE I. Parameters for our DNSs: * Runs A1-A12 use $\alpha = -4, -3.5, -2.5, -1.5, -1, -0.5, 0, 1, 3, 3.5, 4,$ and 5 , respectively. For all the Runs listed in the table, $\Gamma_0 = -0.045$, $\beta = 0.5$, and $\lambda_0 = 3.5$.

$N^2 = 2048^2$ collocation points. We hold λ_0, β , and Γ_0 fixed, and we tune the activity principally by varying α .

In Figs. 1 (a), (b), and (c), we present filled contour plots of the vorticity $\boldsymbol{\omega}(\mathbf{x}, t) = \nabla \times \mathbf{u}(\mathbf{x}, t)$, with some tracers shown via black points, for the representative Runs A1, A8, and D, respectively (see Table I); in Figs. 1 (d)-(i), we give log-log plots versus $k\Lambda$ of the k -shell-averaged energy spectrum $\mathcal{E}(k)$ and energy flux $\Pi(k)$:

$$\begin{aligned} \mathcal{E}(k) &= \frac{1}{2} \sum_{k'=k-1/2}^{k'=k+1/2} \langle \tilde{\mathbf{u}}(\mathbf{k}') \cdot \tilde{\mathbf{u}}(-\mathbf{k}') \rangle_t; \\ \Pi(k) &= -\lambda_0 \sum_{k'=0}^{k'=k} \sum_{k''=k'-1/2}^{k''=k'+1/2} [\langle \tilde{\mathbf{u}}(-\mathbf{k}'') \cdot \mathbf{P}(\mathbf{k}'') \cdot \\ &\quad (\widetilde{\mathbf{u} \cdot \nabla \mathbf{u}})(\mathbf{k}'') \rangle_t]; \end{aligned} \quad (6)$$

here, tildes denote spatial Fourier transforms, $\langle \cdot \rangle_t$ is the time average over the NESS, and the transverse projector $\mathbf{P}(\mathbf{k})$ has the components $P_{ij}(\mathbf{k}) = \delta_{ij} - \frac{k_i k_j}{k^2}$. The total fluid energy, root-mean-square velocity, integral length scale, integral time scale, and integral-scale Reynolds number are, respectively,

$$\begin{aligned} \mathcal{E}_T &= \sum_k \mathcal{E}(k); u_{rms} = \sqrt{2\mathcal{E}_T}; L_I = \frac{\sum_k [\mathcal{E}(k)/k]}{\sum_k \mathcal{E}(k)}; \\ T_I &= L_I/u_{rms}; Re_{L_I} \equiv u_{rms} L_I^3/\Gamma_2. \end{aligned} \quad (7)$$

The gray-shaded areas in Figs. 1 (d)-(i) indicate the ranges of k for which $\nu_{eff}(k) < 0$. For the Runs in Table I, there is no range of k over which $\Pi(k)$ remains constant, unlike its fluid-turbulence counterpart, so we cannot identify inverse- or forward-cascade regimes in $\mathcal{E}(k)$; however, $\mathcal{E}(k)$ is spread over a large range of k and the temporal evolution of \mathbf{u} is chaotic, so the bacterial-turbulence

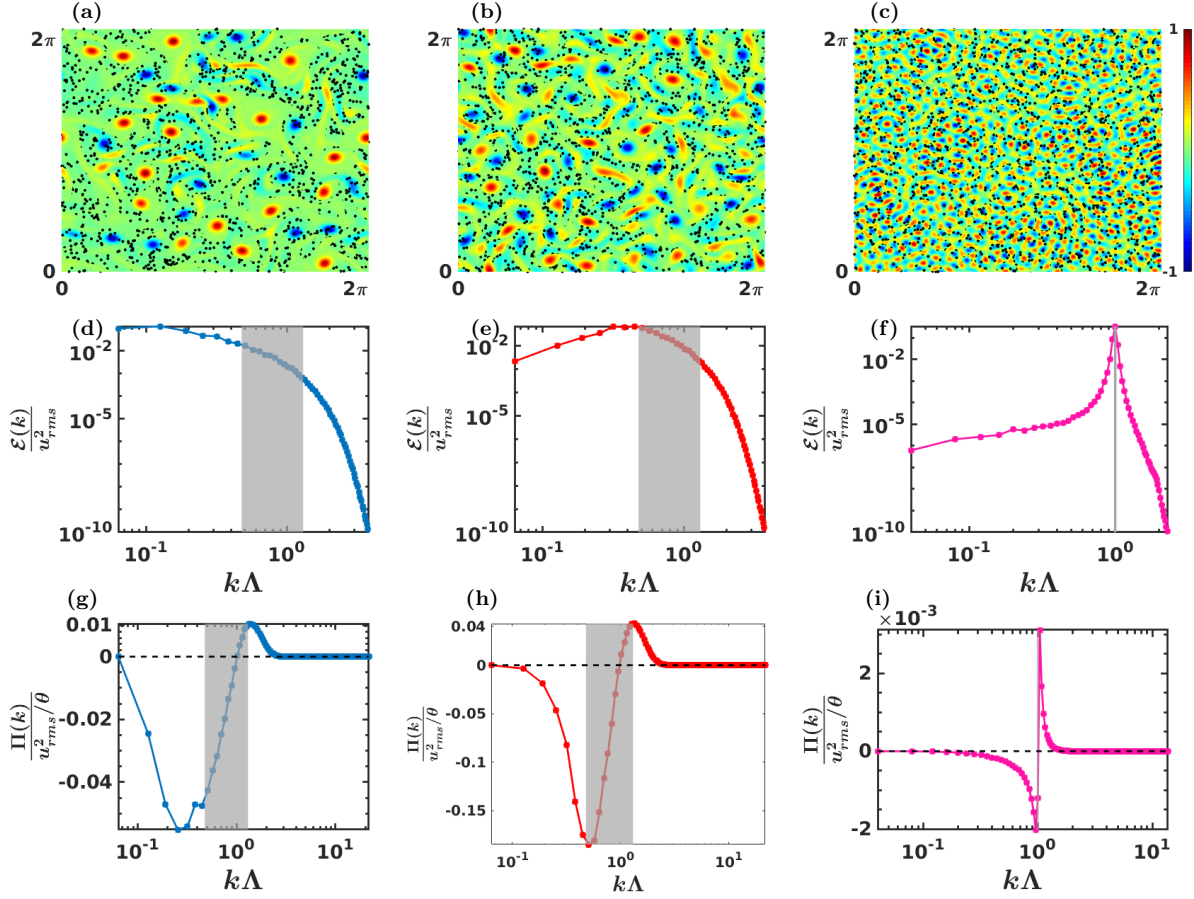


FIG. 1. (Color online) Plots for runs A1, A8, and D (Table I): (a)-(c) Filled contour plots of the vorticity $\omega(\mathbf{x}, t)$, with some tracers (black points), at a representative time in the NESS; log-log (base 10) plots versus $k\Lambda$ of (d)-(f) the energy spectrum $\mathcal{E}(k)$ and (g)-(i) the energy flux $\Pi(k)$ [Eq. (6)]; the gray-shaded areas indicate the ranges of k for which $\nu_{eff}(k) < 0$ [Eq. (5)].

NESS for this model [Eq. (3)] displays spatiotemporal chaos. In Figs. 2 (a)-(d) we present plots versus α of u_{rms}/v_0 , L_I/Λ , T_I/θ , and Re_{L_I} , respectively (Runs A1-A12); as α moves from the *activity regime* ($\alpha < 0$) to the *frictional regime* ($\alpha > 0$), u_{rms}/v_0 , L_I/Λ , and Re_{L_I} decrease, but T_I/θ first decreases and then increases because u_{rms} decreases more rapidly than L_I .

The velocity $\mathbf{v}_L(t)$ of a tracer at $\mathbf{x}_L(t)$ is

$$\frac{d\mathbf{x}_L(t)}{dt} \equiv \mathbf{v}_L(t) = \mathbf{u}(\mathbf{x}_L(t), t). \quad (8)$$

We track $N_p = 10,000$ tracers, employ the second-order Runge-Kutta method for time marching, and evaluate $\mathbf{u}(\mathbf{x}_L(t), t)$ at off-grid points via bilinear interpolation [33–35]; to get good statistics, we use very long runs (3×10^6 time steps per particle).

The acceleration of a tracer particle is

$$\begin{aligned} \mathbf{a}(\mathbf{x}_L, t) &\equiv \frac{\partial \mathbf{u}}{\partial t} + (\mathbf{u} \cdot \nabla) \mathbf{u} \Big|_{\mathbf{x}_L(t)} \\ &= -\nabla P_{eff} - (1 - \lambda_0)(\mathbf{u} \times \boldsymbol{\omega}) \\ &\quad - (\alpha + \beta |u|^2) \mathbf{u} + \Gamma_0 \nabla^2 \mathbf{u} - \Gamma_2 \nabla^4 \mathbf{u} \Big|_{\mathbf{x}_L(t)}, \end{aligned} \quad (9)$$

where the effective pressure $P_{eff} = P - \frac{1}{2}(1 - \lambda_0)\mathbf{u} \cdot \mathbf{u}$; the component of this acceleration along the tracer's trajectory yields a_L , whence we get p_L [Eq. (2)] and its normalized PDF $\mathcal{P}(\frac{p_L}{\langle p_L^2 \rangle^{1/2}})$. From the time series of particle energies (Fig. 4) we obtain the energy-increment PDFs $\mathcal{P}(\frac{W(\tau)}{\langle W^2(\tau) \rangle^{1/2}})$, for various values of $\tau < T_I$. Both these PDFs have zero mean (Figs. 3 (a) and (b)), because we are considering a statistically steady state in which the mean energy input is balanced by dissipation, but

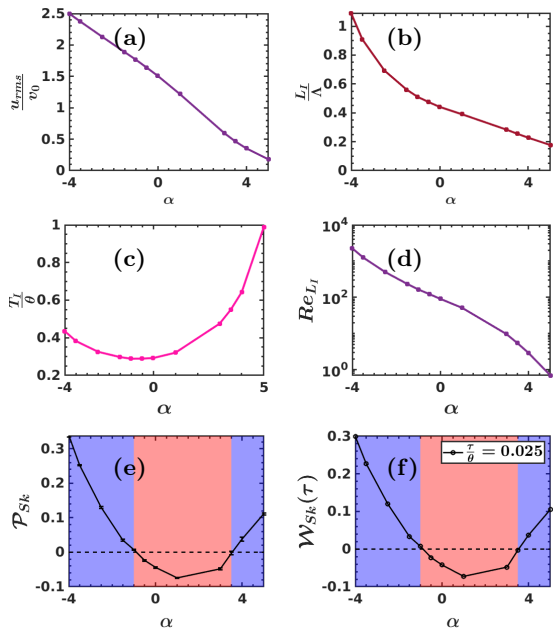


FIG. 2. (Color online) Plots versus α of (a) u_{rms}/v_0 , (b) L_I/Λ , (c) T_I/θ , (d) Re_{L_I} , (e) the skewness \mathcal{P}_{Sk} , and (f) $\mathcal{W}_{Sk}(\tau)$ for $\tau/\theta = 0.025$; in (e) and (f), blue and pink shading indicate, respectively, ranges of α in which the skewnesses are positive and negative.

they are asymmetrical; we characterize this asymmetry by computing the skewnesses

$$\mathcal{P}_{Sk} = \frac{\langle p_L^3 \rangle}{\langle p_L^2 \rangle^{3/2}} \quad \text{and} \quad \mathcal{W}_{Sk}(\tau) = \frac{\langle W^3(\tau) \rangle}{\langle W^2(\tau) \rangle^{3/2}}, \quad (10)$$

which we plot versus α in Figs. 2(e) and (f), respectively. We observe that $\mathcal{P}_{Sk} > 0$ in the large-activity, $\alpha < -2$, and extreme-friction, $\alpha > 3.5$, regions (shaded blue). This is in *stark contrast* to 2D fluid turbulence [3] where $\mathcal{P}_{Sk} < 0$. The values of α for which $\mathcal{P}_{Sk} < 0$ lead to NESSs that are characterized by *flight-crash* events in which, on average, $E(t)$ builds up slowly but decays rapidly. [In 2D Faraday-wave experiments, $\mathcal{P}_{Sk} > 0$ has been attributed to the temporal coherence of these waves, and been removed by filtering [36].] For runs B and D we also find $\mathcal{P}_{Sk} > 0$. In Fig. 4 (a) we plot the time series of $E/\langle E \rangle$ of a typical particle. We also show magnified regions of this time series to exhibit flight-crash events [Fig. 4 (c)], of the types that are predominant in fluid turbulence, and the events in which $E(t)$ builds up faster than it decays [Fig. 4 (b)]. In the large-activity and extreme-friction regions mentioned above, the predominance of the events shown in Fig. 4 (b) leads to $\mathcal{P}_{Sk} > 0$

and, for small τ/θ , $\mathcal{W}_{Sk}(\tau) = \frac{\langle W^3(\tau) \rangle}{\langle W^2(\tau) \rangle^{3/2}} > 0$, because $\lim_{\tau \rightarrow 0} W(\tau, t) \sim p_L(t)$. Furthermore, for $\tau/\theta \ll 1$, we obtain the Taylor-expansion result $\langle W^3(\tau) \rangle \sim \tau^3$, for which we give a representative plot in the inset of Fig. 3 (c). As τ decreases, the tails of $\mathcal{P}(\frac{W(\tau)}{\langle W^2(\tau) \rangle^{1/2}})$ widen, as in fluid turbulence [7][37].

The sign of \mathcal{P}_{Sk} (and, for small τ/θ , the sign of $\mathcal{W}_{Sk}(\tau)$) displays the following correlation with the scale-by-scale energy budget in Fourier space, where we can identify the k -dependence of the energy contributions from the terms with coefficients α , Γ_0 , and λ_0 in Eq. (3). The contributions of the first two terms dominate over those of the third term when $\mathcal{P}_{Sk} > 0$, as we show in detail in the Supplemental Material .

In 2D incompressible flows, the Okubo-Weiss parameter [32, 38–40] distinguishes between vortical and strain-dominated regions. We define this, along particle trajectories, as follows:

$$Q_L(t) = \frac{\omega^2 - \sigma^2}{4} \Big|_{x_L(t)}, \quad (11)$$

where $\omega^2 = \frac{1}{2} \sum_{i,j} (\partial_i u_j - \partial_j u_i)^2$ and $\sigma^2 = \frac{1}{2} \sum_{i,j} (\partial_i u_j + \partial_j u_i)^2$, with $i, j = 1, 2$. $Q_L > 0$ ($\equiv Q_L^+$), in vortical regions, and $Q_L < 0$ ($\equiv Q_L^-$), in strain-dominated regions. The PDF $\mathcal{P}(\frac{Q_L}{\langle Q_L^2 \rangle^{1/2}})$, is positively skewed; its skewness \mathcal{Q}_{Sk} decreases with increasing α , but remains positive throughout the range of α for Runs A1-A12 (inset of Fig. 5 (a)). For high activities, the cumulative PDF $\mathcal{C}(Q_L^+)$, shows a power-law tail for Q_L^+ (Fig. 5 (b)), a unique feature of the bacterial turbulence we study [41]; in contrast, for the high-friction regime ($\alpha > 2$), the tail of $\mathcal{P}(Q_L)$ has a faster-than-exponential decay, for small and positive values of Q_L , as in 2D fluid turbulence. Furthermore, in the large-activity regime $\alpha \leq -2$, the positivity of \mathcal{P}_{Sk} arises from vortical regions, whereas, in the high-friction regime $\alpha \geq 2$, this positive skewness comes from the strain-dominated regions, which we surmise from Fig. 5(c), where we plot \mathcal{P}_{Sk} for the conditioned PDFs $\mathcal{P}(p_L|Q_L^+)$ and $\mathcal{P}(p_L|Q_L^-)$.

Quasi-2D experiments on dense suspension of aerobic bacteria, e.g., *B. subtilis*, show that the average speed of bacterial flow increases with the oxygen concentration [42–44]. We can increase the activity by making α large and negative; in experiments, the activity can be increased by enhanc-

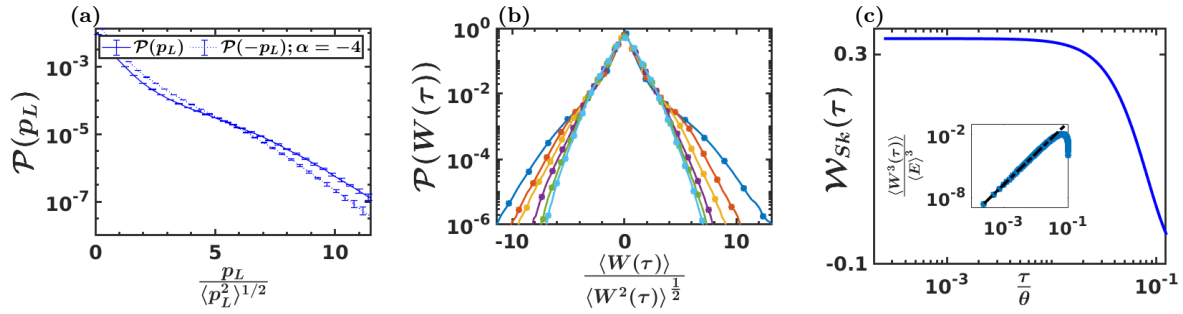


FIG. 3. (Color online) Plots for run B: (a) Semi-log plot of the normalized PDFs (a) $\mathcal{P}(p_L)$ and (b) $\mathcal{P}(W(\tau))$, with τ/θ going from 0.025, 0.08, 0.13, 0.25, 0.38, to 0.50, as we move from the outermost to the innermost curve; in (a) negative values of p_L (dashed) are reflected about the vertical axis to highlight the asymmetry of $\mathcal{P}(p_L)$. (c) Log-Log (base 10) plot versus τ/θ of the skewness $\mathcal{W}_{Sk}(\tau)$. Inset: for the same range of τ/θ , a log-log plot versus τ/θ of $\langle W^3(\tau) \rangle / \langle E \rangle^3$; the dashed black line is a fit to $\langle W^3(\tau) \rangle / \langle E \rangle^3 \sim (\tau/\theta)^3$.

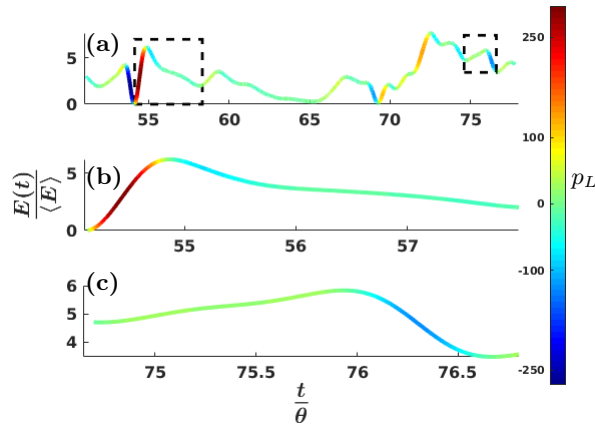


FIG. 4. (Color Online) Plot of the normalised energy $E(t)/\langle E \rangle$ versus the normalized time t/θ along a representative particle trajectory from Run A1; the colors along the trajectory indicate the value of p_L .

ing the oxygen, because the polar-ordered velocity scale $v_p = \sqrt{\frac{|\alpha|}{\beta}}$ is a measure of the swimming speed of bacteria; $u_{rms} \propto \alpha$ (cf. [45]); and in the frictional or $\alpha > 0$ regime, the value of α can be tuned in experiments by changing the bottom friction or the air-drag-induced friction (see the Supplemental Material for details). Therefore, experiments on dense bacterial suspensions should be able to examine irreversibility in bacterial turbulence as a function of the activity as we have done in Fig. 2.

It is important to use the methods we describe here to explore irreversibility of bacterial turbulence in other models [19, 23, 24] and also in models for active fluids [46, 47] and active nemat-

ics [26, 27, 48]. We propose to carry out such studies in the near future.

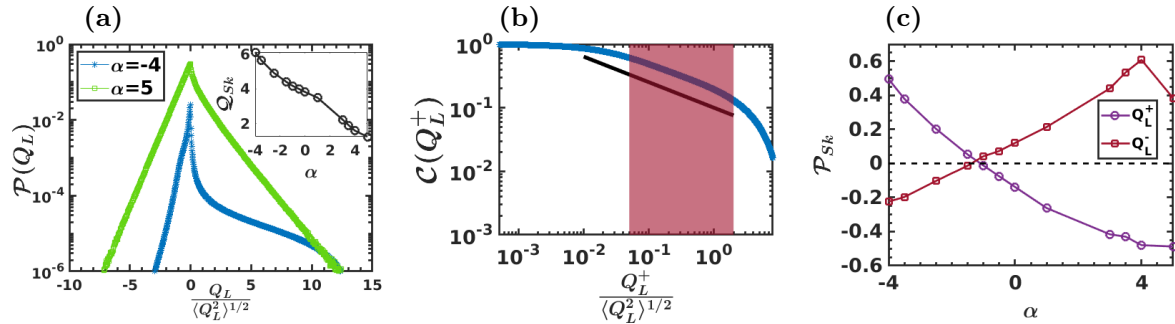


FIG. 5. (Color online) (a) Semi-log plots of $\mathcal{P}(Q_L)$ for runs A1 (blue) and A13 (green). Inset gives the plot versus α of skewness, Q_{Sk} , for $\mathcal{P}(Q_L)$. (b) Log-log plot of $\mathcal{C}(Q_L^+)$ for run A1; the shaded region shows a power-law and the solid black line gives the fit $\mathcal{C}(Q_L^+) \sim [Q_L^+]^{-\vartheta}$, with $\vartheta = 0.37 \pm 0.04$. (c) Plots versus α of \mathcal{P}_{Sk} for the conditioned PDFs (see text) $\mathcal{P}(p_L|Q_L^+)$ (violet) and $\mathcal{P}(p_L|Q_L^-)$ (maroon).

SUPPLEMENTAL MATERIAL

In this Supplementary Material we provide details of the following:

1. Our direct numerical simulations (DNSs).
2. Different contributions to the energy spectrum and the role of the advective term.
3. The effects of filtering on the statistics of the power p_L .
4. Additional figures and tables.

Direct Numerical Simulation (DNS)

For two dimensional (2D) incompressible flows we rewrite Eq. 3, in the main paper, in terms of the vorticity field $\boldsymbol{\omega}(\mathbf{x}, t)$ as follows:

$$\frac{\partial \boldsymbol{\omega}}{\partial t} + \lambda_0 \mathbf{u} \cdot \nabla \boldsymbol{\omega} = -\alpha \boldsymbol{\omega} - \beta \nabla \times (|\mathbf{u}|^2 \mathbf{u}) + \Gamma_0 \nabla^2 \boldsymbol{\omega} - \Gamma_2 \nabla^4 \boldsymbol{\omega}; \quad (12)$$

and we define the stream function $\Psi(\mathbf{x}, t)$ in terms of which

$$\mathbf{u} = \nabla \times \Psi \hat{\mathbf{z}} \text{ and } \boldsymbol{\omega} = -\nabla^2 \Psi, \quad (13)$$

where $\hat{\mathbf{z}}$ is the unit vector perpendicular to the plane containing \mathbf{u} . Our DNS of Eqs. (12) and (13) employs a pseudospectral method [32, 49]; we use a square simulation domain, with sides of length $L = 2\pi$, periodic boundary conditions in all directions, and $N \times N$ collocation points distributed uniformly over this domain. In most of our simulations we use

$N = 1024$; we have checked in representative simulations that our results are not altered significantly if we use $N = 2048$. We employ the second-order Runge-Kutta integrating-factor method IFRK2 for time marching [50]. We have developed a CUDA Fortran code for our DNSs which are executed on K20 and K80 GPUs. Once our DNS yields a turbulent, but statistically steady, state, we introduce N_p Lagrangian particles and follow their trajectories. The position $\mathbf{x}_L(t)$ of such a particle evolves as follows:

$$\frac{d\mathbf{x}_L(t)}{dt} \equiv \mathbf{v}_L(t) = \mathbf{u}(\mathbf{x}_L(t), t).$$

We integrate Eq. (14) by using the second-order Runge-Kutta scheme and bi-linear interpolation to obtain the particle velocity $\mathbf{v}_L(t)$ at off-grid points. We evolve each particle trajectory for 3×10^6 time steps; and we store \mathbf{x}_L , \mathbf{v}_L , the particle acceleration \mathbf{a}_L , and the power p_L after every 50 iterations.

We follow Refs. [15, 45] in restricting our model parameters to experimentally realizable regimes. The average velocities observed in experiments on *B. subtilis* are $\simeq 25 \mu\text{m/s}$, at normal oxygen concentrations; the typical viewing area is $400 \mu\text{m} \times 400 \mu\text{m}$; we map these to the constant velocity scale v_0 and the simulation box area $L \times L$, respectively. This gives us the scale factors of $25/v_0$ and $4 \times 10^{-2}/L$ for mapping velocities and lengths, respectively, in our DNS to their experimental counterparts: specifically, v_0 , v_p , and u_{rms} are, respectively, $\simeq 25 \mu\text{m/s}$, $\simeq (25 \mu\text{m/s} \text{ to } 70 \mu\text{m/s})$ and $\simeq (4.5 \mu\text{m/s} \text{ to } 65 \mu\text{m/s})$; similarly, Λ , which sets the linear scale for vortical regions, $\simeq 25 \mu\text{m}$.

Energy budget

For the shell-averaged energy spectrum

$$\mathcal{E}(k) = \frac{1}{2} \sum_{k'=k-1/2}^{k'+k+1/2} \langle \tilde{\mathbf{u}}(\mathbf{k}') \cdot \tilde{\mathbf{u}}(-\mathbf{k}') \rangle_t \quad (14)$$

we have [22]

$$\begin{aligned} \partial_t \mathcal{E}(k) &= T^a(k) - T^c(k) - 2\alpha \mathcal{E}(k) \\ &\quad - 2\Gamma_0 k^2 \mathcal{E}(k) - 2\Gamma_2 k^4 \mathcal{E}(k), \end{aligned} \quad (15)$$

where $T^a(k)$ and $T^c(k)$, the k -shell averaged contributions from the advective and cubic terms in Eq. (12), respectively, are

$$\begin{aligned} T^a(k) &= -\lambda_0 \sum_{k'=k-1/2}^{k'+k+1/2} \langle \tilde{\mathbf{u}}(-\mathbf{k}') \cdot \mathbf{P}(\mathbf{k}') \cdot (\widetilde{\mathbf{u} \cdot \nabla \mathbf{u}})(\mathbf{k}') \rangle_t \\ T^c(k) &= \beta \sum_{k'=k-1/2}^{k'+k+1/2} \langle \tilde{\mathbf{u}}(-\mathbf{k}') \cdot \mathbf{P}(\mathbf{k}') \cdot (\widetilde{|\mathbf{u}|^2 \mathbf{u}})(\mathbf{k}') \rangle_t, \end{aligned} \quad (16)$$

with $P_{ij}(\mathbf{k}) = \delta_{ij} - \frac{k_i k_j}{k^2}$ the transverse projector and $\langle \cdot \rangle_t$ the average over time t . The flux of energy arising from the advective term is

$$\Pi(k) = - \sum_{k'=0}^{k'=k} T^a(k'). \quad (17)$$

The effective viscosity

$$k^2 \nu_{eff}(k) = (\alpha + 2\beta u_{rms}^2 + \Gamma_0 k^2 + \Gamma_2 k^4)$$

can be used to rewrite Eq. (12), in a form that resembles the Navier-Stokes, with the constant viscosity ν replaced by $\nu_{eff}(k)$. To obtain Eq. (5), we use the approximation $T^c(k) \simeq -4\beta u_{rms}^2 \mathcal{E}(k)$ suggested in Ref. [22]; here, u_{rms} must be obtained from our calculation. Clearly, the wave numbers k at which energy is injected (dissipated) are those with $\nu_{eff}(k) < 0$ (> 0).

The sign of \mathcal{P}_{Sk} (and, for small τ/θ , the sign of $\mathcal{W}_{Sk}(\tau)$) displays the following correlation with the scale-by-scale energy budget in Fourier space, where we can identify the k -dependence of the energy contributions from the terms with coefficients α , Γ_0 , and $T^a(k)$ from Eq. (15) and (16), which we show in Fig. (3): the contribution to the energy budget (15) from the active term, $-2\alpha \mathcal{E}(k)$, is significantly greater than $T^a(k)$, for values of $\alpha < -2$. For values of $\alpha > 2$, where $\mathcal{P}_{Sk} > 0$, the other active term, $-2\Gamma_0 k^2 \mathcal{E}(k)$ dominates over $T^a(k)$.

Averaging and Filtering

For conventional 2D fluid turbulence, the effects of different types of forcing, in both DNSs and experiments, on \mathcal{P}_{Sk} have been discussed in Refs. [3, 51], where it is noted that Faraday-wave experiments yield $\mathcal{P}_{Sk} > 0$; this sign is attributed to the temporal coherence of Faraday waves. It is shown in Ref. [3] that, if p_L is averaged over a time that is comparable to this coherence time, then $\mathcal{P}_{Sk} < 0$; this averaging filters high-frequency components in $p_L(t)$. Specifically, they use

$$\bar{p}_L(t) = \frac{1}{\mathcal{T}} \int_0^{\mathcal{T}} p_L(t+t') dt'; \quad (18)$$

\mathcal{T} , the time over which $p_L(t)$ is averaged, is taken to be a multiple (typically 0.5 – 5) of the forcing-correlation time. In the mean-bacterial-velocity model, which we consider, there is no external forcing; the natural counterpart of \mathcal{T} in Eq. (18) is the particle-acceleration time τ_a that we can obtain from the first zero-crossing of the normalised autocorrelation function

$$C_a(\tau) = \frac{\langle a_L(t) a_L(t+\tau) \rangle}{\langle a_L(t) a_L(t) \rangle}, \quad (19)$$

which we plot in the inset of Fig. 7 (a) for different values of α . In Fig. 7 (a) we show that τ_a increase monotonically with α . We define the smoothing parameter

$$sm(\tau_a) \equiv \frac{\mathcal{T}}{\tau_a}, \quad (20)$$

the multiple of τ_a over which we average $p_L(t)$. In Fig. 7 (b) we plot \mathcal{P}_{Sk} versus α for $sm(\tau_a) = 1$ (solid line) and $sm(\tau_a) = 4$ (dashed line); for values of $\mathcal{P}_{Sk} > 0$ (in both high-activity and high-friction regimes), the averaging defined in Eq. 18 leads to a change in the sign of \mathcal{P}_{Sk} for values of $sm(\tau_a) > 1$. This averaging does not change the sign of \mathcal{P}_{Sk} if the unaveraged $p_L(t)$ leads $\mathcal{P}_{Sk} < 0$. This is also evident from the PDFs of the filtered \bar{p}_L ; we present representative plots for the PDFs for runs A1 and A8 in Figs. 8 (a) and (b), respectively. From Figs. 7 and 8 we conclude that the fast-gain-slow-loss events, shown in Fig. 4 of the main text, are filtered out by the averaging procedure, which we have described above, because these events occur over time scales that are $\simeq \tau_a$.

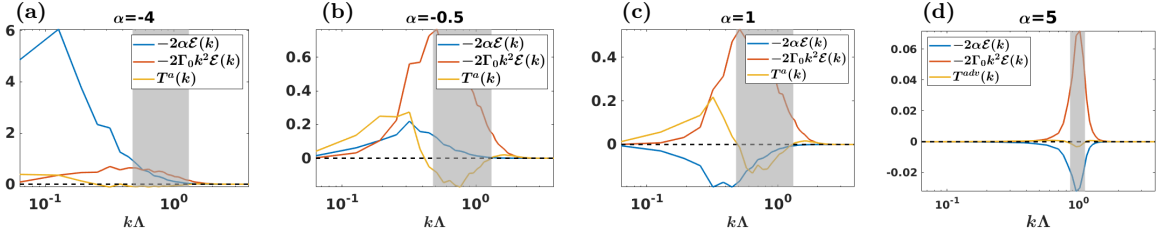


FIG. 6. (Color online) Semi-log plots versus $k\Lambda$ of $T^\alpha(k)$ (yellow), $-2\alpha\mathcal{E}(k)$ (blue) and $-2\Gamma_0k^2\mathcal{E}(k)$ (orange); the gray-shaded areas indicate the ranges of k for which $\nu_{eff}(k) < 0$ for (a) run A1, (b) run A7, (c) run A8 and (d) run A11

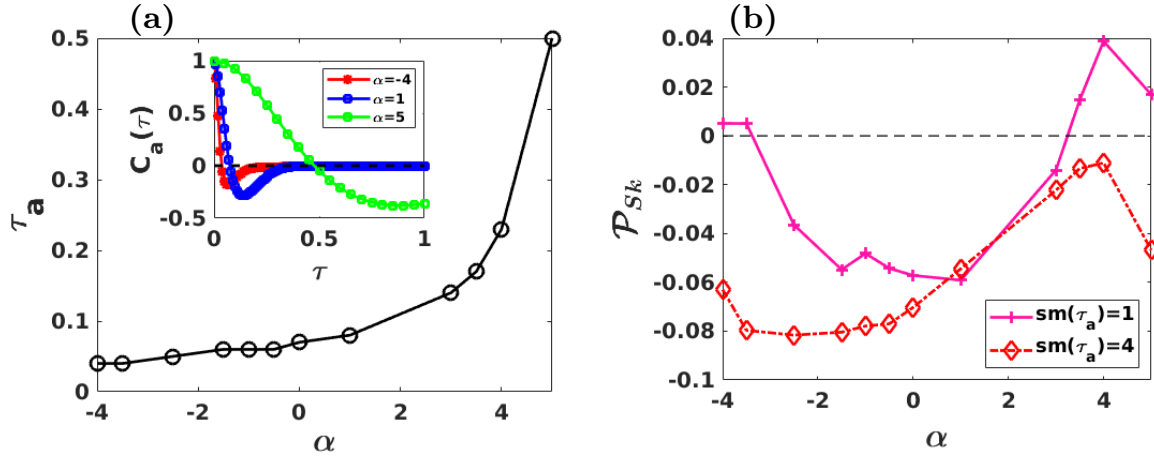


FIG. 7. (Color online) (a) Plot versus α of the acceleration-autocorrelation time τ_a ; the inset shows $C_a(\tau)$ as a function of τ , for $\alpha = -4$ (blue), $\alpha = 1$ (red), and $\alpha = 5$ (green). (b) Plots versus α of \mathcal{P}_{Sk} for $sm(\tau_a) = 1$ (solid line) and $sm(\tau_a) = 4$ (dashed line).

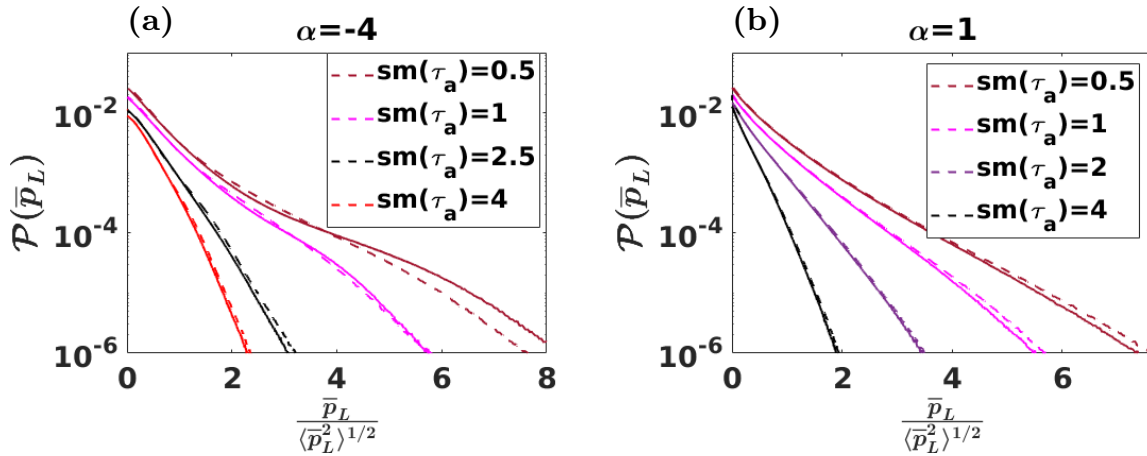


FIG. 8. Semi-log plots of the PDFs $\mathcal{P}(\bar{p}_L)$ for different values $sm(\tau_a)$ for (a) Run A1 and (b) Run A8.

Supplemental Tables and Figures

- In Table II we list the parameters for Run D in the main paper.
- In Fig. 9 we plot various moments of p_L versus α for Runs A1-A12.
- In Figs. 10 and 11 we present representative plots for Runs C and D.

Run	u_{rms}	L_I	T_I	\mathcal{P}_{Sk}
D	8.8e-2	4e-2	0.45	1.2e-2

TABLE II. DNS values of u_{rms} , L_I , T_I and \mathcal{P}_{Sk} for Run D.

- In Fig. 12 we give a plot of the local slope in the power-law regime in $\mathcal{C}(Q_L^+)$ for Run A1.

Acknowledgments

We thank J.K. Alageshan, V. Deshpande (NVIDIA), N.B. Padhan, S. Shukla, and S.S.V. Kolluru for discussions, CSIR, the National Supercomputing Mission (NSM), and SERB (India) for support, and SERC (IISc) for computational resources.

* kollurukiran@iisc.ac.in

† agupta@phy.iith.ac.in

‡ akvermajnusps@gmail.com

§ rahul@iisc.ac.in

- [1] U. Frisch, *Turbulence: the legacy of AN Kolmogorov* (Cambridge university press, 1995).
- [2] H. Rose and P. Sulem, Fully developed turbulence and statistical mechanics, *Journal de Physique* **39**, 441 (1978).
- [3] H. Xu, A. Pumir, G. Falkovich, E. Bodenschatz, M. Shats, H. Xia, N. Francois, and G. Boffetta, Flight-crash events in turbulence, *Proceedings of the National Academy of Sciences* **111**, 7558 (2014).
- [4] J. Jucha, H. Xu, A. Pumir, and E. Bodenschatz, Time-reversal-symmetry breaking in turbulence, *Physical review letters* **113**, 054501 (2014).
- [5] M. Chertkov, A. Pumir, and B. I. Shraiman, Lagrangian tetrad dynamics and the phenomenology of turbulence, *Physics of fluids* **11**, 2394 (1999).
- [6] H. Xu, A. Pumir, and E. Bodenschatz, Lagrangian view of time irreversibility of fluid turbulence, *Science China Physics, Mechanics & Astronomy* **59**, 1 (2016).
- [7] A. Pumir, H. Xu, E. Bodenschatz, and R. Grauer, Single-particle motion and vortex stretching in three-dimensional turbulent flows, *Physical review letters* **116**, 124502 (2016).
- [8] G. Falkovich and A. Frishman, Single flow snapshot reveals the future and the past of pairs of particles in turbulence, *Physical review letters* **110**, 214502 (2013).
- [9] A. Bhatnagar, A. Gupta, D. Mitra, and R. Pandit, Heavy inertial particles in turbulent flows gain energy slowly but lose it rapidly, *Physical Review E* **97**, 033102 (2018).
- [10] K. Pietrzyk, J. A. Horwitz, F. M. Najjar, and R. W. Minich, On analysis and stochastic modeling of the particle kinetic energy equation in particle-laden isotropic turbulent flows, *Physics of Fluids* **34**, 013316 (2022).
- [11] J. R. Picardo, A. Bhatnagar, and S. S. Ray, Lagrangian irreversibility and eulerian dissipation in fully developed turbulence, *Physical Review Fluids* **5**, 042601 (2020).
- [12] S. S. Ray, Non-intermittent turbulence: Lagrangian chaos and irreversibility, *Physical Review Fluids* **3**, 072601 (2018).
- [13] P. Švančara and M. La Mantia, Flight-crash events in superfluid turbulence, *Journal of Fluid Mechanics* **876** (2019).
- [14] A. K. Verma, S. Shukla, V. Shukla, A. Bhatnagar, and R. Pandit, Heavy inertial particles in superfluid turbulence: Coflow and counterflow, *arXiv preprint arXiv:2110.09801* (2021).
- [15] H. H. Wensink, J. Dunkel, S. Heidenreich, K. Drescher, R. E. Goldstein, H. Löwen, and J. M. Yeomans, Meso-scale turbulence in living fluids, *Proceedings of the National Academy of Sciences* **109**, 14308 (2012).
- [16] J. Dunkel, S. Heidenreich, M. Bär, and R. E. Goldstein, Minimal continuum theories of structure formation in dense active fluids, *New Journal of Physics* **15**, 045016 (2013).
- [17] J. Dunkel, S. Heidenreich, K. Drescher, H. H. Wensink, M. Bär, and R. E. Goldstein, Fluid dynamics of bacterial turbulence, *Physical review letters* **110**, 228102 (2013).
- [18] J. Słomka and J. Dunkel, Generalized navier-stokes equations for active suspensions, *The European Physical Journal Special Topics* **224**, 1349 (2015).
- [19] M. Linkmann, G. Boffetta, M. C. Marchetti, and B. Eckhardt, Phase transition to large scale coherent structures in two-dimensional active matter turbulence, *Physical review letters* **122**, 214503 (2019).
- [20] M. Linkmann, M. C. Marchetti, G. Boffetta, and B. Eckhardt, Condensate formation and multi-scale dynamics in two-dimensional active suspensions, *Physical Review E* **101**, 022609 (2020).
- [21] J. Słomka and J. Dunkel, Spontaneous mirror-symmetry breaking induces inverse energy cascade in 3d active fluids, *Proceedings of the National Academy of Sciences* **114**, 2119 (2017).
- [22] V. Bratanov, F. Jenko, and E. Frey, New class of turbulence in active fluids, *Proceedings of the National Academy of Sciences* **112**, 15048 (2015).

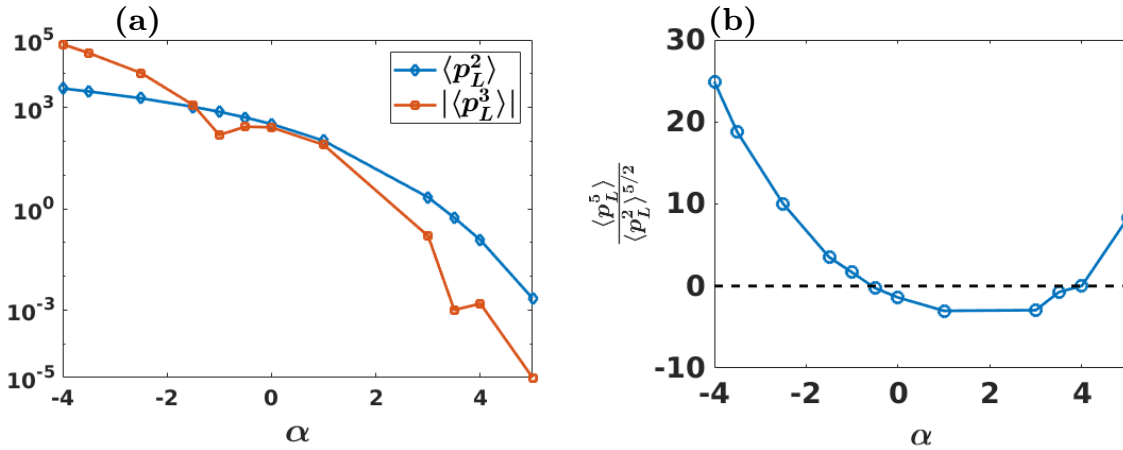


FIG. 9. For Runs A1-A12 (Table I in the main paper): (a) Absolute values of the third moment $|\langle p_L^3 \rangle|$ and the second moment $\langle p_L^2 \rangle$ plotted versus α . (b) Plots of the normalized fifth moment versus α ; these can also be used to quantify irreversibility and to draw the same conclusions as we have in the main paper.

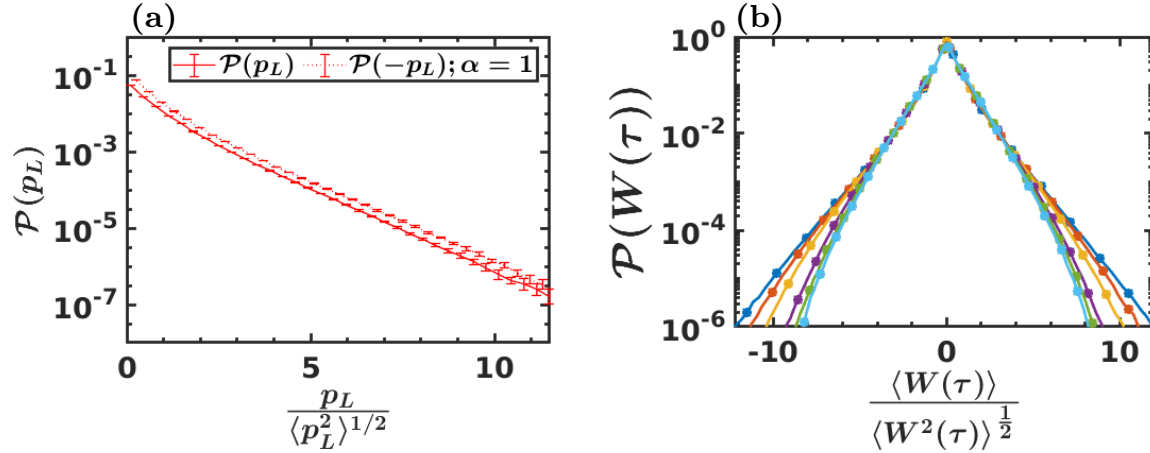


FIG. 10. (Color online) Plots for Run C: (a) Semi-log plot of the normalized PDF $\mathcal{P}(p_L)$; negative values of p_L (dashed) are reflected about the vertical axis to highlight the asymmetry of $\mathcal{P}(p_L)$. (b) Semi-log plots of $\mathcal{P}(W(\tau))$, for $\tau/\theta = 0.025, 0.08, 0.13, 0.25, 0.38$ and 0.50 (outermost to innermost curve).

- [23] A. U. Oza, S. Heidenreich, and J. Dunkel, Generalized swift-hohenberg models for dense active suspensions, *The European Physical Journal E* **39**, 1 (2016).
- [24] N. Rana and P. Perlekar, Coarsening in the two-dimensional incompressible toner-tu equation: Signatures of turbulence, *Physical Review E* **102**, 032617 (2020).
- [25] R. Alert, J. Casademunt, and J.-F. Joanny, Active turbulence, *Annual Review of Condensed Matter Physics* **13** (2021).
- [26] S. P. Thampi, R. Golestanian, and J. M. Yeomans, Velocity correlations in an active nematic, *Physical review letters* **111**, 118101 (2013).
- [27] S. Thampi and J. Yeomans, Active turbulence in active nematics, *The European Physical Journal*

Special Topics **225**, 651 (2016).

- [28] M. Bär, R. Großmann, S. Heidenreich, and F. Peruani, Self-propelled rods: Insights and perspectives for active matter, *Annual Review of Condensed Matter Physics* **11**, 441 (2020).
- [29] Equation (3) is not Galilean invariant; it reduces to the Navier-Stokes equation with friction for $\Gamma_0 > 0, \alpha > 0, \Gamma_2 = 0, \lambda_0 = 1$, and $\beta = 0$.
- [30] This is similar to energy injection in the Kuramoto-Sivashinsky equation see, e.g., Refs. [52–54].
- [31] M. James, W. J. Bos, and M. Wilczek, Turbulence and turbulent pattern formation in a minimal model for active fluids, *Physical Review Fluids* **3**, 061101 (2018).

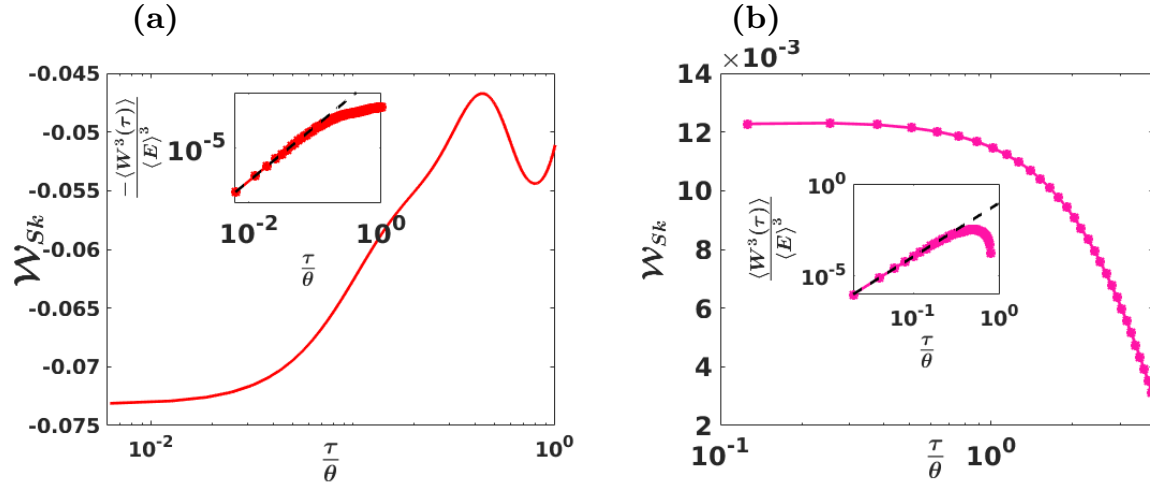


FIG. 11. (Color online) Log-Log (base 10) plot versus τ/θ of the skewness $W_{Sk}(\tau)$. Inset: for the same range of τ/θ , a log-log plot versus τ/θ of $\langle W^3(\tau) \rangle / \langle E \rangle^3$; the dashed black line is a fit to $\langle W^3(\tau) \rangle / \langle E \rangle^3 \sim (\tau/\theta)^3$ for (a) Run C and (b) Run D.

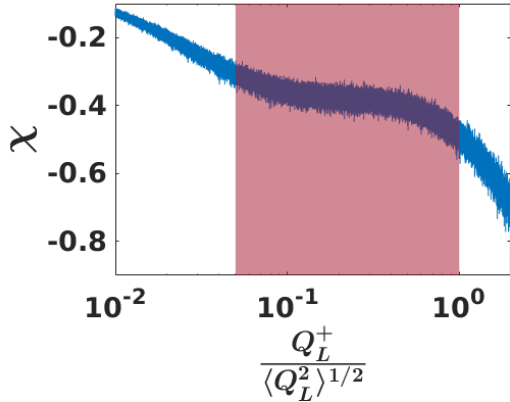


FIG. 12. For Run A1, semi-log plot of the local slope χ of $\mathcal{C}(Q_L^+)$ in the shaded region that shows a power law.

[32] P. Perlekar, S. S. Ray, D. Mitra, and R. Pandit, Persistence problem in two-dimensional fluid turbulence, *Physical review letters* **106**, 054501 (2011).
 [33] M. James and M. Wilczek, Vortex dynamics and lagrangian statistics in a model for active turbulence, *The European Physical Journal E* **41**, 1 (2018).
 [34] S. Mukherjee, R. K. Singh, M. James, and S. S. Ray, Anomalous diffusion and lévy walks distinguish active from inertial turbulence, *Phys. Rev. Lett.* **127**, 118001 (2021).
 [35] R. K. Singh, S. Mukherjee, and S. S. Ray, Lagrangian manifestation of anomalies in active turbulence, arXiv preprint arXiv:2112.00667 (2021).

[36] For conventional 2D fluid turbulence, Refs. [3, 51] discuss, for both DNSs and experiments, the effects of different types of forcing on \mathcal{P}_{Sk} ; they report $\mathcal{P}_{Sk} < 0$ in DNSs with white-noise forcing; by contrast, in Faraday-wave experiments, they observe $\mathcal{P}_{Sk} > 0$, which they attribute to the temporal coherence of Faraday waves. In the latter case they employ a filtering procedure that again yields $\mathcal{P}_{Sk} < 0$. In the Supplemental Material we investigate the effects of a similar filtering procedure for 2D bacterial turbulence in Eq. (3).
 [37] This widening could be a signature of intermittency effects, which we examine elsewhere [55].
 [38] A. Okubo, Horizontal dispersion of floatable particles in the vicinity of velocity singularities such as convergences, in *Deep sea research and oceanographic abstracts*, Vol. 17 (Elsevier, 1970) pp. 445–454.
 [39] J. Weiss, The dynamics of enstrophy transfer in two-dimensional hydrodynamics, *Physica D: Nonlinear Phenomena* **48**, 273 (1991).
 [40] L. Giomi, Geometry and topology of turbulence in active nematics, *Physical Review X* **5**, 031003 (2015).
 [41] Similar PDFs have been obtained in Ref. [35], but the power-law form has not been noted.
 [42] L. H. Cisneros, J. O. Kessler, S. Ganguly, and R. E. Goldstein, Dynamics of swimming bacteria: Transition to directional order at high concentration, *Phys. Rev. E* **83**, 061907 (2011).
 [43] A. Sokolov, I. S. Aranson, J. O. Kessler, and R. E. Goldstein, Concentration dependence of the collective dynamics of swimming bacteria, *Phys. Rev. Lett.* **98**, 158102 (2007).

- [44] A. Sokolov and I. S. Aranson, Physical properties of collective motion in suspensions of bacteria, *Phys. Rev. Lett.* **109**, 248109 (2012).
- [45] C. P. Sanjay and A. Joy, Friction scaling laws for transport in active turbulence, *Phys. Rev. Fluids* **5**, 024302 (2020).
- [46] R. Chatterjee, N. Rana, R. A. Simha, P. Perlekar, and S. Ramaswamy, Inertia drives a flocking phase transition in viscous active fluids, *Physical Review X* **11**, 031063 (2021).
- [47] M. J. Bowick, N. Fakhri, M. C. Marchetti, and S. Ramaswamy, Symmetry, thermodynamics and topology in active matter, arXiv preprint arXiv:2107.00724 (2021).
- [48] R. Alert, J.-F. Joanny, and J. Casademunt, Universal scaling of active nematic turbulence, *Nature Physics* **16**, 682 (2020).
- [49] C. Canuto, M. Y. Hussaini, A. Quarteroni, A. Thomas Jr, *et al.*, *Spectral methods in fluid dynamics* (Springer Science & Business Media, 2012).
- [50] S. M. Cox and P. C. Matthews, Exponential time differencing for stiff systems, *Journal of Computational Physics* **176**, 430 (2002).
- [51] A. Pumir, H. Xu, G. Boffetta, G. Falkovich, and E. Bodenschatz, Redistribution of kinetic energy in turbulent flows, *Physical Review X* **4**, 041006 (2014).
- [52] Y. Kuramoto and T. Tsuzuki, Persistent propagation of concentration waves in dissipative media far from thermal equilibrium, *Progress of theoretical physics* **55**, 356 (1976).
- [53] G. I. Sivashinsky, Nonlinear analysis of hydrodynamic instability in laminar flames—i. derivation of basic equations, *Acta astronautica* **4**, 1177 (1977).
- [54] D. Roy and R. Pandit, One-dimensional kardar-parisi-zhang and kuramoto-sivashinsky universality class: Limit distributions, *Physical Review E* **101**, 030103 (2020).
- [55] K. Kolluru, A. Gupta, A. Verma, and R. Pandit, To be published.